Breakaway oxidation of austenitic stainless steels induced by alloyed sulphur

C. Pascal [a,b,*], V. Parry [a,b], E. Fedorova [c], M. Braccini [a,b], P. Chemelle [d], N. Meyer [d], D. Oquab [e], D. Monceau [e], Y. Wouters [a,b], M. Mantel [a,b,d]

[a] Univ. Grenoble Alpes, SIMAP, F-38000 Grenoble, France
[b] CNRS, SIMAP, F-38000 Grenoble, France
[c] Polytechnic Institute of Siberian Federal University, Krasnoyarsk, Russia
[d] UGITECH SA, Ugine, France
[e] Université de Toulouse, Institut Carnot CIRIMAT, ENSIACET, Toulouse, France

Keywords:
A. Stainless steel
B. Raman spectroscopy
B. SEM
C. Kinetic parameters
C. Internal oxidation
C. High temperature corrosion

A B S T R A C T

This work focuses on the effect of alloyed sulphur as MnS inclusions in austenitic stainless steels. AISI 304L and AISI 303 were oxidized at 1000 °C in synthetic air. The high sulphur grade, AISI 303, presents a breakaway oxidation with formation of nodules with an inner part composed of alternated layers of Fe-rich and Cr-rich oxides. During oxidation, MnS inclusions near the metal/oxide interface are partially dissociated. Manganese is incorporated in the oxide. The sulphur is trapped in Cr,Mn-oxysulphide aggregates which formation leads to a local decrease of the Cr concentration and consequently to the formation of non-protective Fe-rich oxide.

1. Introduction

Austenitic stainless steels are probably the most important class of corrosion resistant metallic materials. Their good corrosion properties depend on two factors: a high Cr content that is responsible for the protective oxide layer formation and a high Ni content allowing the steel remaining austenitic. Thus, the base composition is normally a Fe–Cr–Ni alloy. In practice, the situation is much more complex with several other elements being present, such as Mo, Mn, C, N, S among others.

Sulphur is added to improve steels machinability. Sulphur is considered as a detrimental element for welding and hot ductility which is essential for forging and rolling. In order to avoid iron sulphides formation (FeS) which are non-deformable harmful inclusions, Mn is added to precipitate S as manganese sulphides (MnS) in the liquid state during solidification. These inclusions exhibit better mechanical properties at high temperature than FeS. The MnS precipitates are elongated during hot rolling processes and act as lubricant and allow chips breaking by promoting localized shearing stress during machining [1].

Sulphur addition is also known to have detrimental effects on adhesion of thermally grown alumina (Al_2O_3) [2–10] and chromia (Cr_2O_3) [11,12] scales after isothermal or cyclic oxidation tests. Sulphur has a strong tendency to segregate on free surfaces such as voids formed beneath the oxide scale from vacancy coalescence due to outward diffusion of cations during oxide scale growth. Surface free energy is then lowered leading to a more favourable nucleation and growth of voids to cavities [12]. Although failure mechanisms due to S segregation are pretty well understood for alumina scales, things remain unclear for chromia forming alloys for which presence of S at the metal/oxide interface of well adhesive oxide scales has been reported [7]. Interfacial morphology associated with growth stresses seems to be a major cause of scale breakdown of chromia scale, S segregation remaining a secondary effect [7,13].

The present work focuses on the effect of S on the oxidation behaviour of austenitic stainless steels under severe experimental conditions. Although the initial microstructure and chemical composition of the chosen alloys are very close except for S content, their oxidation behaviour differs strongly. Experimental results are supported by thermodynamic calculations allowing an estimate of the free S content and investigating the MnS precipitates stability. Finally, the differences in oxidation behaviour and consequently in microstructure development are discussed.

* Corresponding author at: Univ. Grenoble Alpes, SIMAP, F-38000 Grenoble, France.
E-mail address: Celine.Pascal@simap.grenoble-inp.fr (C. Pascal).

2. Materials and methods

Austenitic stainless steels, AISI 304L (EN 1.4307) and AISI 303 (EN 1.4305), were provided by Ugitech France. These alloys were produced by continuous casting. Bars of about 22 mm in diameter, shaped by hot rolling, were cold drawn with a 15% reduction of the section. Their chemical compositions, reported in Table 1, were controlled by fluorescence spectroscopy analysis and optical emission spectrometry equipped with a gas analyzer. According to Table 1, their close compositions, except for S content, made these two alloys good candidates for the present study.

Optical micrographs of the as-received alloys are displayed in Fig. 1. Since the alloys were cold drawn without subsequent annealing, the elongated microstructure resulting from the hot rolling stage is retained. The grain size of 20–30 μm is similar for both alloys.

MnS "stringers", appearing in black in Fig. 1, can be observed in a greater amount in AISI 303 since the S content in this alloy is about ten times higher than in AISI 304L (2950 ppmw and 250 ppmw for AISI 303 and AISI 304L respectively). These MnS inclusions, highly deformable at the temperature of the rolling process (1000–1300 °C), are oriented in the working direction of the bar. Elongated residual δ-ferrite related to an incomplete transformation in γ-austenite during solidification is also observed in grey in Fig. 1.

Rectangular samples of about 20 mm long, 10 mm width and 2 mm thick were cut in the longitudinal direction of the bars by electrical discharge machining. Before oxidation experiments, samples were ground with SiC paper down to a final grade 1200, ultrasonically cleaned with ethanol and accurately weighed and sized.

Isothermal thermogravimetric experiments (TGA) were performed in two SETARAM™ TAG 24S thermobalances equipped with a double symmetrical furnace that permits to limit perturbations resulting from gas flow, buoyancy, and convection. This symmetrical furnace provides a very stable signal and minimizes the drift error to less than 1 μg/h. The samples were heated at 60 °C/min up to 1000 °C, isothermally oxidized during 50 h and cooled down to room temperature at 60 °C/min in a synthetic air flow (20% O_2 – 80% N_2; 0.6 L/h i.e. a linear flow about 2 mm/s at RT). Additional experiments were performed to check that the gas flow was not the limiting step of the overall oxidation process of samples. TGA allows measuring the mass gain related to the oxide scale growth as a function of time but also the mass losses due to possible oxide scale spallation during cooling.

Discontinuous oxidation tests in synthetic air flow (20% O_2 – 80% N_2; 0.6 L/h) were also performed in a tubular furnace. The heating rate was set to 60 °C/min. The cooling happens in the switched off furnace. Cross-sections were prepared for chemical and microstructural investigations. Samples coated with an electrochemical nickel layer were mounted and polished with diamond paste up to 1 μm. Final polishing was achieved with colloidal silica suspension. SEM investigations were performed on top surface and on cross-section of the oxidized samples with a FEG SEM coupled with EDS analysis (FEG SEM 7001F JEOL). The chemical composition and the crystallographic structure of the oxide scales were also investigated using Raman spectroscopy (Renishaw RM1000).

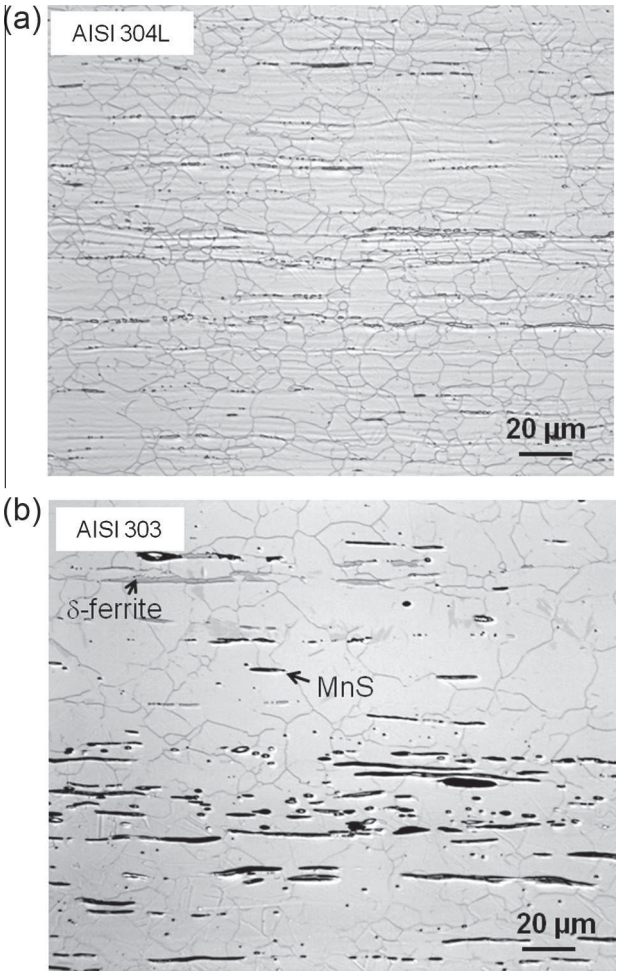

Fig. 1. Optical micrographs of the AISI 304L and AISI 303 substrates after electrolytic etching in 85% nitric acid revealing the MnS sulphides (black), the residual δ-ferrite (grey) and the grain size.

3. Results and discussion

3.1. Oxidation kinetics and microstructure

Isothermal kinetic curves of the two austenitic stainless steels oxidized for 50 h at 1000 °C under synthetic air are displayed in Fig. 2. Three tests were performed on AISI 304L and AISI 303 samples. For both austenitic steels, differences are observed during the early stages of oxidation. The transition from initial linear behaviour to subsequent parabolic behaviour takes place after about 10 h with the establishment of the stationary stage of oxidation limited by diffusion. After the transient stage, the parabolic constants, k_p, can be calculated with the complete parabolic law, given by Eq. (1) [14].

$$t = A + B \cdot \frac{\Delta m}{S} + \frac{1}{k_p} \cdot \left(\frac{\Delta m}{S}\right)^2 \quad (1)$$

Table 1
Chemical compositions of austenitic stainless steels AISI 304L and AISI 303 (wt.%).

wt.%	Fe	Ni	Cr	Mn	Si	C	S	N	O	Ca
AISI 304L	Bal.	8.960	18.040	1.128	0.458	0.021	0.025	0.048	0.010	0.005
AISI 303	Bal.	8.284	17.100	1.746	0.443	0.055	0.295	0.035	0.015	0.013

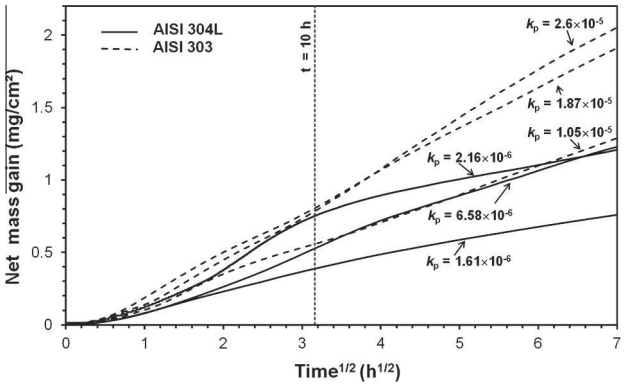

Fig. 2. Net mass gain per surface unit area (in mg/cm^2) *versus* square root of oxidation time (in h$^{1/2}$) for three AISI 304L and AISI 303 samples oxidized at 1000 °C under flowing synthetic air. Values of parabolic rate constants, k_p (in mg^2/cm^4/s), are calculated with Eq. (1) between 10 and 50 h.

where t is the time, A and B are constants and ($\Delta m/S$) is the mass change of the sample per unit area. The complete parabolic law allows calculation of the « true » parabolic constant, i.e. the parabolic constant which is given by the diffusion through the oxide layer, even after a transient regime with different oxidation kinetics.

Parabolic constant after the transient regime, from 10 to 50 h, lies between 1.6×10^{-6} and 6.6×10^{-6} mg^2/cm^4/s for the three AISI 304L samples, in good agreement with literature [15,16], whereas it varies between 1.1×10^{-5} and 2.6×10^{-5} mg^2/cm^4/s for the three AISI 303 samples, i.e. about five times larger in average.

Plot of the net mass change per surface unit area as function of temperature allowing the observation of spallation events occurring during cooling steps is displayed in Fig. 3. Buoyancy effect was corrected according to the method described by Raffaitin et al. [17]. The Archimedes equation was fitted on the mass curve during cooling, using the volume difference between the sample and the counterweight reference sample (symmetrical TGA) as an adjustable parameter. Cooling was preferred to heating because less oxidation is expected during cooling, especially below 800 °C. Then, this fitted equation was applied to the entire mass signal. After the correction of buoyancy effect, slight variations of the mass during the beginning of the heating ramp, which are due to the difference of temperature between the two furnaces of the symmetrical arrangement, were also corrected.

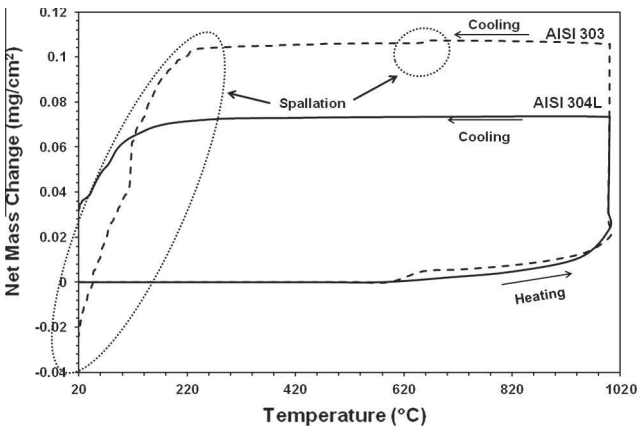

Fig. 3. Net mass change per surface unit area (in mg/cm^2) after buoyancy correction as a function of temperature (in °C) for AISI 304L and AISI 303 oxidized for 50 h at 1000 °C under flowing synthetic air (heating rate = cooling rate = 60 °C/min).

The curves of the net mass change vs. temperature, in Fig. 3, show that oxidation started during heating for both alloys. 20% of the overall net mass gain occurred during heating between 600 °C and 1000 °C and 80% occurred during the isothermal stage at 1000 °C for 50 h. During isothermal stage, the net mass gain was higher for AISI 303 than for AISI 304L.

Spallation events happened during cooling especially for AISI 303. For this alloy, a first event took place at about 700 °C and extensive spallation occurred below 220 °C. Visual observations of this sample after cooling showed a large extent of spalling area. For AISI 304L, a lower spallation, confirmed by visual observations, was evidenced during cooling at about 220 °C.

These results clearly evidence the better oxidation resistance of AISI 304L compared to AISI 303. These results are not in agreement with Yurek et al. investigations were cyclic oxidation experiments at 900 °C in pure oxygen of rapidly solidified 303 and wrought 304 stainless steels were performed [18]. This may be explained by different Si contents and grain sizes of the as-received alloys. In Yurek et al. work, better oxidation behaviour and scale adhesion of AISI 303 are probably linked with mechanical keying by SiO_2 intrusions and smaller grain size. In the present study, grain sizes and Si contents are similar for both steels. The higher oxidation resistance of AISI 304L is confirmed by cyclic thermogravimetric experiments (CTGA) carried out in synthetic air flow at 1000 °C [19].

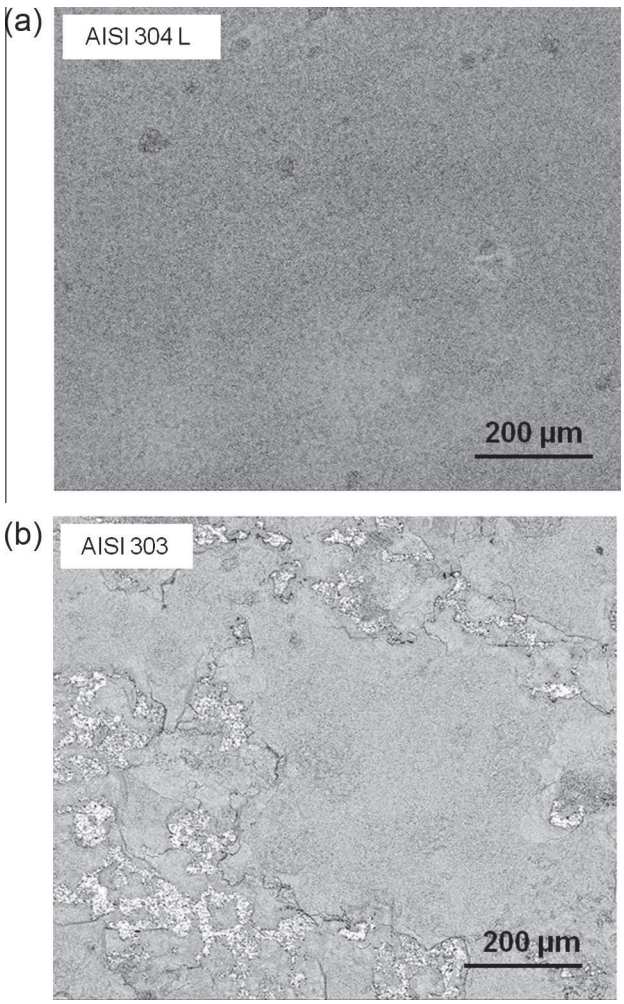

Fig. 4. Surface SEM micrographs in BSE mode of the oxide scale thermally grown on AISI 304L (a) and AISI 303 (b) for 50 h at 1000 °C under flowing synthetic air.

Surface SEM views in BSE mode of the AISI 304L and AISI 303 oxide scales isothermally grown for 50 h at 1000 °C under synthetic air flow are displayed in Fig. 4(a) and (b) respectively. The morphologies of the two scales are different. While the oxide scale grown on AISI 304L seems relatively homogeneous, the oxide scale grown on AISI 303 seems brittle and partially spalled. The white areas correspond to the spalled part of the oxide scale whereas the grey zones are related to the unaltered oxide. This result is in good agreement with thermogravimetric tests showing extensive spalling events during cooling for AISI 303 sample.

According to surface EDS analysis of oxide scale grown on AISI 303 (not presented), oxygen level is high in the spalled region indicating that spallation does not take place at the metal/oxide interface. The oxide scale contains Fe, Cr and Mn and its outer layer is richer in Fe.

Raman spectra, carried out on the surface of the AISI 304L and AISI 303 samples after oxidation at 1000 °C during 50 h in synthetic air, are displayed in Fig. 5. For AISI 304L, chromia Cr_2O_3 and solid solution $(Fe,Cr)_2O_3$ as well as spinel $MnCr_2O_4$ are present in the scale [20]. For AISI 303, different spectra are recorded depending on the analyzed zone: Fe-rich spinel type oxide $(Fe,Cr)_3O_4$ and Fe-rich corundum type oxide Fe_2O_3 and $(Fe,Cr)_2O_3$. The variation of the composition may be related to spallation: the Fe-rich spinel type spectra corresponding to unaltered region and the Fe-rich corundum type spectra corresponding to spalled area.

From Raman and EDS analyses, the Fe content in the oxide scale grown on AISI 303 is higher than in the scale grown on AISI 304L which is consistent with the TGA curves trends since Fe-rich oxides are known to be less protective than Cr-rich oxide scales.

SEM cross-sections and EDS maps of the oxide scale isothermally grown on AISI 304L for 50 h at 1000 °C under synthetic air are displayed in Fig. 6. According to Fig. 6(a), the oxide scale is continuous with a thickness of about 4–5 µm and presents a wavy-shaped and adhesive interface with the substrate. According to Fig. 6(b), the oxide scale is duplex. The external part (orange in Fig. 6(b)) consists in faceted crystals rich in Cr and Mn, probably the spinel type oxide $(Fe,Cr,Mn)_3O_4$ labelled in Raman spectroscopy. The internal part (green in Fig. 6(b) and yellow in Fig. 6(c)) is Fe,Cr-rich oxide with an increasing content of Cr from the surface to the bulk. According to Raman spectroscopy, these phases may be labelled as corundum type solid solution $(Fe,Cr)_2O_3$ and Cr_2O_3. Internal oxidation of Si is also observed (yellow in Fig. 6(b)). The silica layer (SiO_2) is discontinuous with large intrusions along the alloy grain boundaries which have been already observed in literature [11,18]. Concerning the bulk, a Cr depletion zone, about 10–15 µm thick, is observed below the metal/oxide interface, with an

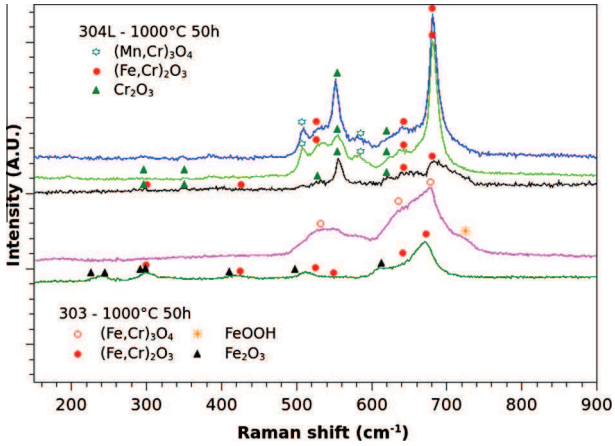

Fig. 5. Raman spectra of oxide scales isothermally grown on AISI 303 and AISI 304L for 50 h at 1000 °C under flowing synthetic air.

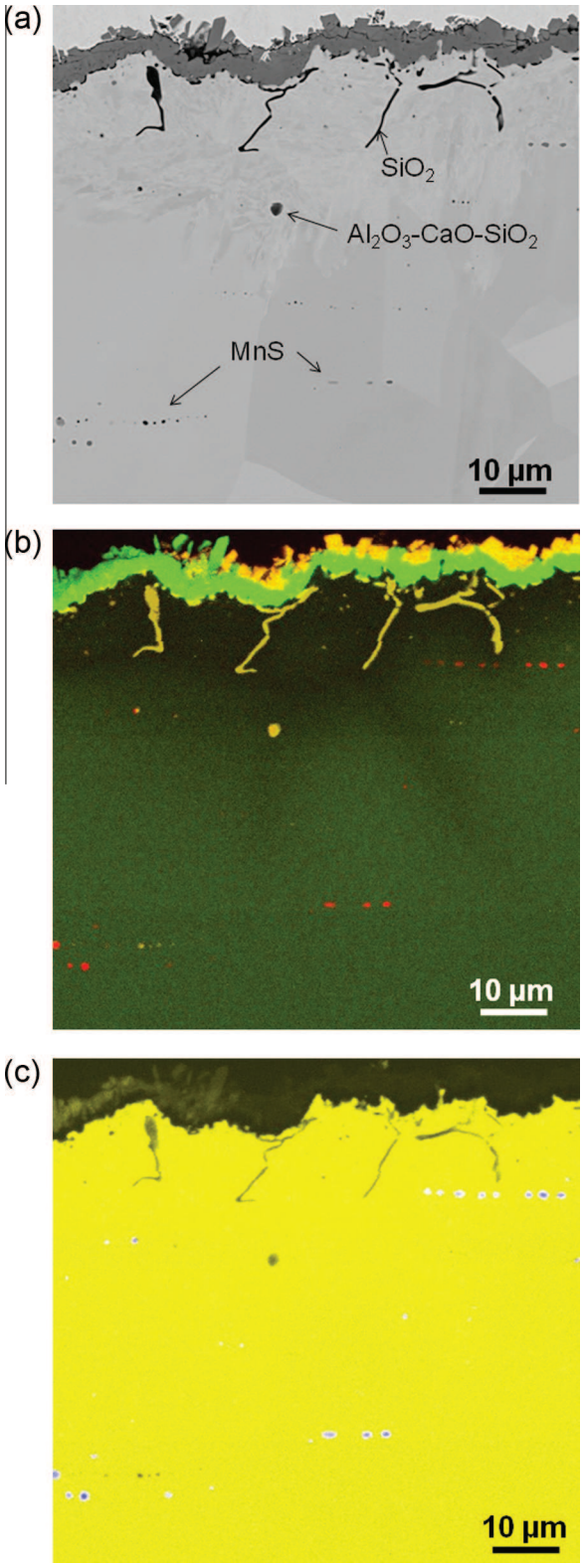

Fig. 6. Oxide scale thermally grown on AISI 304L for 50 h at 1000 °C under flowing synthetic air: (a) BSE SEM cross-section micrograph, (b) EDS map with Cr K_α in green, Mn K_α in red, Si K_α in yellow, Cr + Mn in orange and (c) EDS map with Fe K_α in yellow, S K_α in blue. (For interpretation of the references to colour in this figure legend, the reader is referred to the web version of this article.)

enhancement along the grain boundaries. MnS inclusions (red and blue in Fig. 6(b) and (c) respectively) oriented perpendicularly to the cross-section are also noticed. These MnS inclusions were

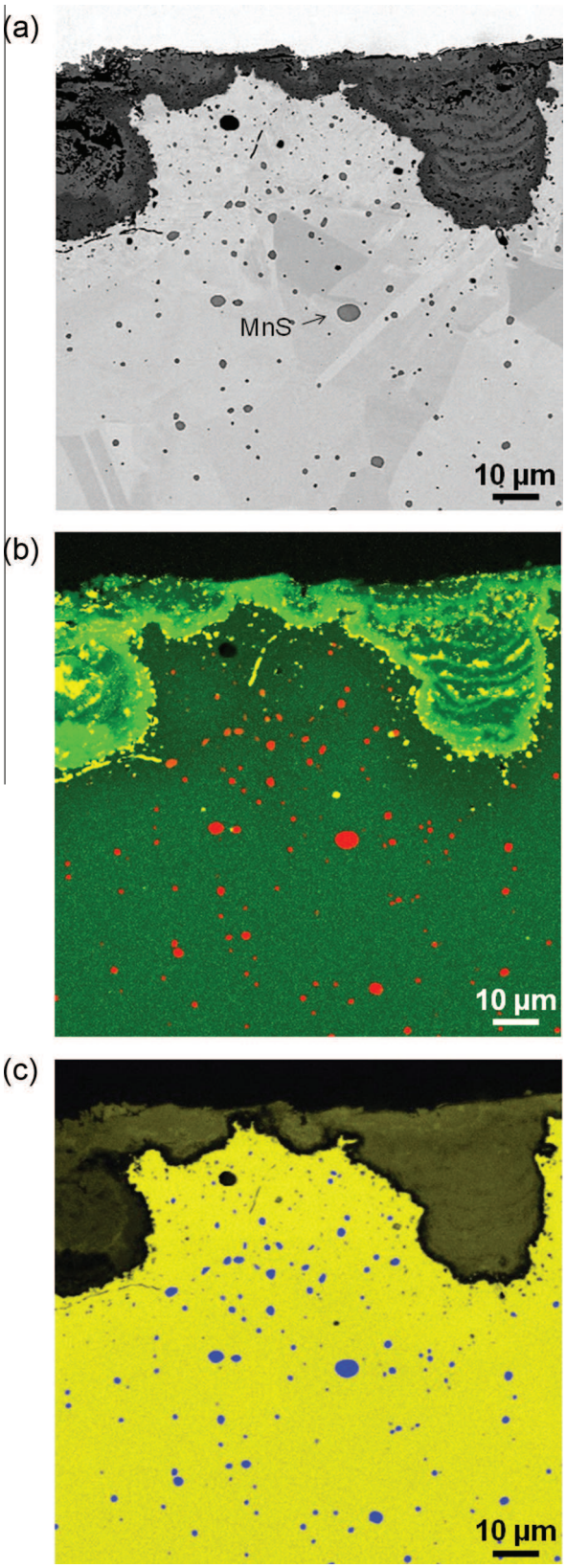

Fig. 7. Oxide scale thermally grown on AISI 303 for 50 h at 1000 °C under flowing synthetic air: (a) BSE SEM cross-section micrograph, (b) EDS map with Cr K_α in green, Mn K_α in red, Si K_α in yellow, Cr + Mn in orange and (c) EDS map with Fe K_α in yellow, S K_α in blue. (For interpretation of the references to colour in this figure legend, the reader is referred to the web version of this article.)

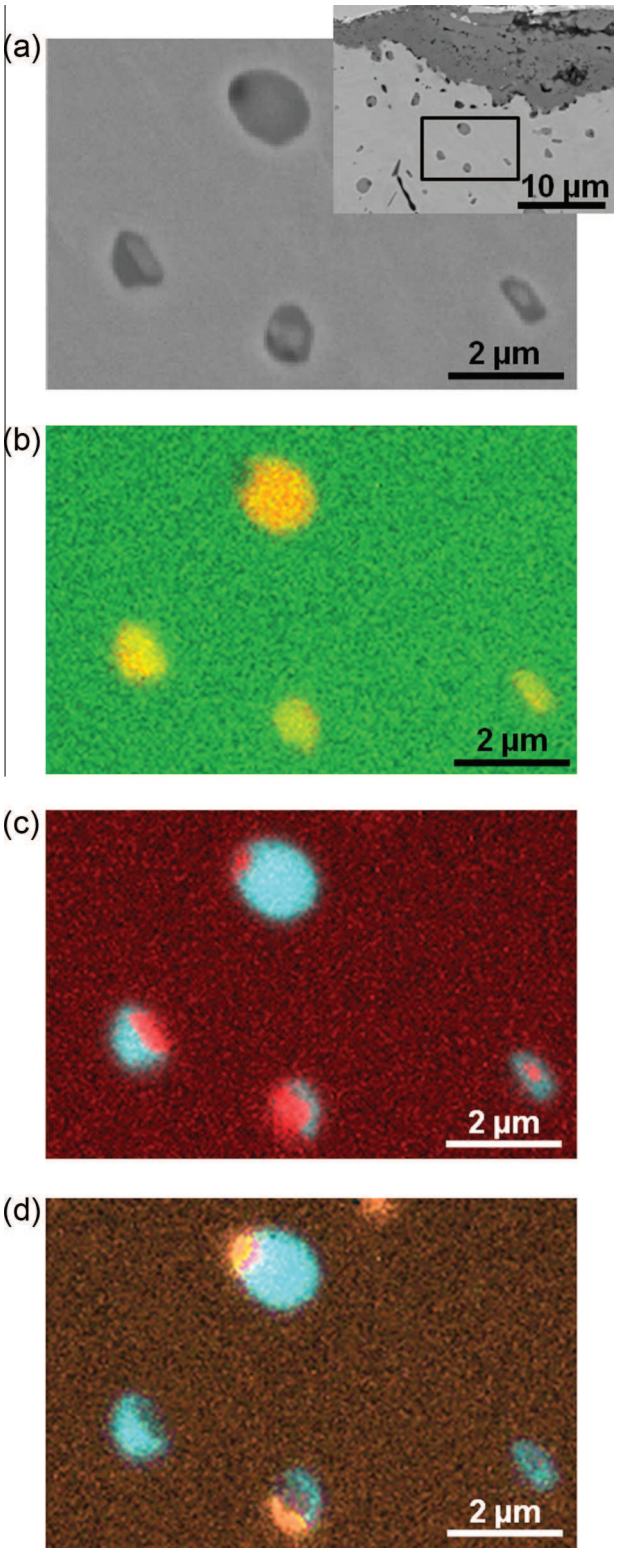

Fig. 8. EDS maps of S containing precipitates in the bulk close to the metal/oxide interface in AISI 303 after oxidation at 1000 °C for 50 h in synthetic air flow: (a) BSE Mode, the inset details the position of the precipitates regarding the metal/oxide interface (b) Cr K_α in green, Mn K_α in red, Cr + Mn in orange, (c) O K_α in red, S K_α in blue and (d) Si K_α in orange, S K_α in blue. (For interpretation of the references to colour in this figure legend, the reader is referred to the web version of this article.)

already present in the bulk before oxidation (Fig. 1). Few alumino-silicate lime inclusions (Al_2O_3–CaO–SiO_2) present during the steel process are also observed.

Thus microstructural characterizations evidence that AISI 304L exhibits a fairly protective duplex oxide scale with an outer $(Mn,Fe,Cr)_3O_4$ spinel layer and an inner Cr-rich $(Cr,Fe)_2O_3$ corundum layer. The features of this oxide scale are usual for chromia forming stainless steel and are fully described in literature [16,21,22].

SEM cross-section micrograph and EDS maps of the oxide scale isothermally grown on AISI 303 for 50 h at 1000 °C under synthetic air are displayed in Fig. 7. According to Fig. 7(a), the oxide layer is uneven and heterogeneous with large pits of oxides penetrating the bulk on about 20 μm in depth. The oxidation pits are composed of repeated sequential layers of a Fe,Cr-rich oxide (green and yellow in Fig. 7(b) and (c) respectively) and a discontinuous layer of SiO_2 (yellow in Fig. 7(b)). For each stacks, the Cr content in the Fe,Cr-rich oxide varies with a higher level close to the silica layer (dark grey/green in Fig. 7(a) and (b) respectively). A continuous 2–3 μm thick Cr-rich layer underlined by discontinuous silica layer borders the metal/oxide interface. Conversely to the observations made on AISI 304L, silica intrusions into the alloy grains boundaries are not evidenced. Moreover, Mn-rich oxide is not observed even if its formation is expected in the external part of the oxide scale. Mn-rich oxide has probably been removed during extensive spalling occurring during cooling and also during metallographic preparation of the cross-section.

This inner scale morphology lies on the competition between chromium and iron oxides formation which is characteristic of breakaway oxidation Chromia is thermodynamically the most stable oxide but iron oxides grow faster The formation of the chromia layer requires a minimum flux of Cr from the underlying alloy to the zone of oxide formation. If the Cr flux is not sufficient to form a continuous chromia scale, the faster growing Fe oxides will continue to grow leading to the formation of Fe-rich nodules on the sample surface [23]. Grain boundaries are high diffusivity paths and can supply sufficient Cr flux in the regions where the grain boundaries meet the alloy surface. However, in regions away from the grain boundaries, the Cr flux depends on much slower volume diffusion [11,18].

However, at the base of the oxide nodules, Cr concentration can reach a level high enough to sustain the growth of a continuous chromia healing layer which inhibits further growth of the nodules and causes a decrease of the oxidation rate. When the bulk Cr concentration decreases over again, the healing layer breaks down. The repeat of this mechanism leads to the formation of layered oxide scale with alternated Fe-rich and Cr-rich oxides. According to Evans et al. [24], about 16 wt.% in Cr is required at the alloy/scale interface to form a healing layer at 750–900 °C. Basu and Yurek [11] consider that 18 wt.% in Cr is close to the borderline composition at which nodule formation ceases. Cr concentrations of the as-received alloys seem very close to these concentration limits. Nevertheless, metal grain size [25] and Si content [26] play a significant role on the Cr critical value for a given temperature. The critical Cr content was found to range from 10 to 13 wt.% in Fe–Cr alloy systems oxidized in dry air, which may vary with oxidation temperature, atmosphere and alloying elements [27].

It is also generally admitted that Si addition decreases the probability of breakaway oxidation. First, during the initial stages of oxidation, internal precipitates of silica form, which sustains internal precipitates of chromia settlement. Silica, being more stable than chromia, forms as internal precipitates beneath the chromia scale and the discontinuous layer of silica acts as a partial diffusion barrier and leads to a decrease in the oxidation rate [11,18]. MnS precipitates in the bulk have been reported to influence the morphology of the silica phase formed during oxidation by providing nucleation sites for internal oxidation of Si [18,28].

Fig. 8 presents EDS maps of S containing precipitates in the bulk close to the metal/oxide interface. The composition of the former MnS inclusions is altered near the interface. A Cr, Si and O enrichments of the inclusions are evidenced. These observations highlight formation of two-phase aggregates in the alloy near the oxide scale which consist of Cr, Si-rich oxides and Mn, Cr-rich sulphides. These aggregates will be called Cr,Mn-oxysulphides in the following.

The volume fraction of S containing precipitates for AISI 303 is high since the S content in this alloy is about ten times higher than in AISI 304L (red and blue in Fig. 7(b) and (c) respectively).

Image processing of S EDS map allows the study of the evolution of the area number density and size of S containing precipitates in the bulk near the metal/oxide interface. Area measurements and particle counting on the binarized image were processed with Image J software [29]. About 570 precipitates were studied over an area of about 85 μm thick from the interface. Mean area and area number density values were calculated from 5 μm

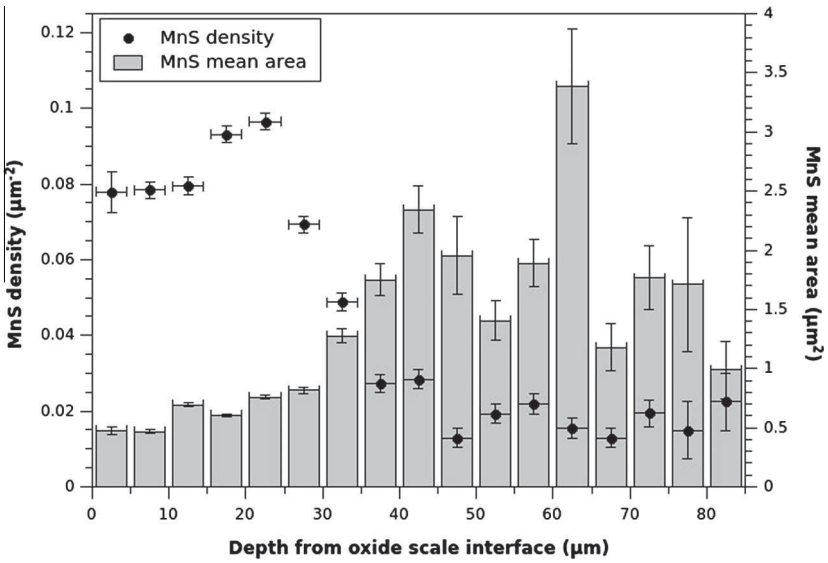

Fig. 9. Area number density (in μm^{-2}) and mean area (in μm^2) of S containing precipitates in AISI 303 as a function of distance (in μm) from steel/oxide interface after oxidation at 1000 °C for 50 h in synthetic air flow.

Table 2
Free S calculations for AISI 304L and AISI 303 alloys using CEQCSI [30] and Thermo-Calc with TCFE6 database [32,33].

Alloys	S (ppmw)	Mn (wt%)	Ca (ppmw)	MnS (%)	CaS (%)	Free S (ppmw) CEQCSI	Free S (ppmw) Thermo-Calc
AISI 304L	250	1.128	50	97.7	2.3	4.2	~0.01
AISI 303	2950	1.746	130	99.8	0.2	6.1	~0.01

depth slices. Results are presented in Fig. 9. The bulk region broadens from a distance of about 50 μm below the interface. Only 20% of the studied precipitates are located is this region which may explain the scattered values. The precipitates area number density is stable and around 0.02 unit.μm^{-2} and the mean area varies between 1 and 2.5 μm^2. Between 5 and 30 μm below the metal/oxide interface, the precipitates density is four to five times higher than in the bulk whereas their mean area is lower and around 0.5 μm^2.

The increase in number and decrease in size of the S containing precipitates close to the metal/oxide interface suggest the dissociation of the MnS inclusions near the metal/oxide interface during thermal processing. This phenomenon has already been observed by Basu and Yurek [11], the growth of the outer Mn containing spinel layer providing the driving force for this dissociation. Mn diffuses to the metal/oxide interface and is incorporated in the oxide scale whereas S can diffuse into the alloy and precipitates with other sulphide former elements. This point will be discussed in the following section.

The experimentally observed oxidation and Cr enrichment of sulphides tends to confirm the reprecipitation hypothesis. The oxygen partial pressure, $p(O_2)$, is sufficient to internally oxidize Cr and Si and sulphides act as nucleation sites for internal oxidation of Si [18,28].

3.2. Sulphur content effect

Although the chemical compositions and the initial microstructure of AISI 304L and AISI 303 are very close, the oxidation behaviour of the two alloys differs strongly. In our experimental conditions, AISI 303 presents catastrophic oxidation behaviour with a high oxidation rate, a high net mass gain and severe spalling events during cooling. Since the S content is about ten times higher for the AISI 303 (Table 1), the differences observed can be discussed regarding the S content through the role of MnS inclusions and the amount of free S in the alloys.

The free S is the S which is not tied up with sulphide forming elements such as Mn, Ca, Cr or Ti. This S, in solid solution, is free to diffuse towards interfaces where it can segregate and possibly embrittle the material. Free S content is estimated using thermodynamic calculations with software and database such as Thermo-Calc or CEQCSI. CEQCSI (Chemical Equilibrium Calculations for the Steel Industry) is a home-built model describing metallic phases in equilibrium with oxide and sulphide inclusions [30]. Thermo-Calc has been developed in the framework of the CALPHAD approach [31,32], in which thermodynamic data of each phase is described through the Gibbs free energy giving the possibility to model multi-component phase diagrams. Thermo-Calc database, TCFE6 [33], only takes into account MnS and FeS when CEQSI is upgraded with CaS, CrS, TiS and oxysulphides that may precipitate in the liquid, therefore gives much less free S than CEQSI calculations. Results of thermodynamic calculations are presented in Table 2. Free S content is very low and similar for both alloys suggesting that the free S content is independent of the S level in the alloy. Sulphur is mainly tied up in the very stable MnS sulphides as observed in the bulk in Figs. 6 and 7. The free S amount cannot explain the observed differences of oxidation behaviour. Contrary to alumina forming alloy, free S accumulation

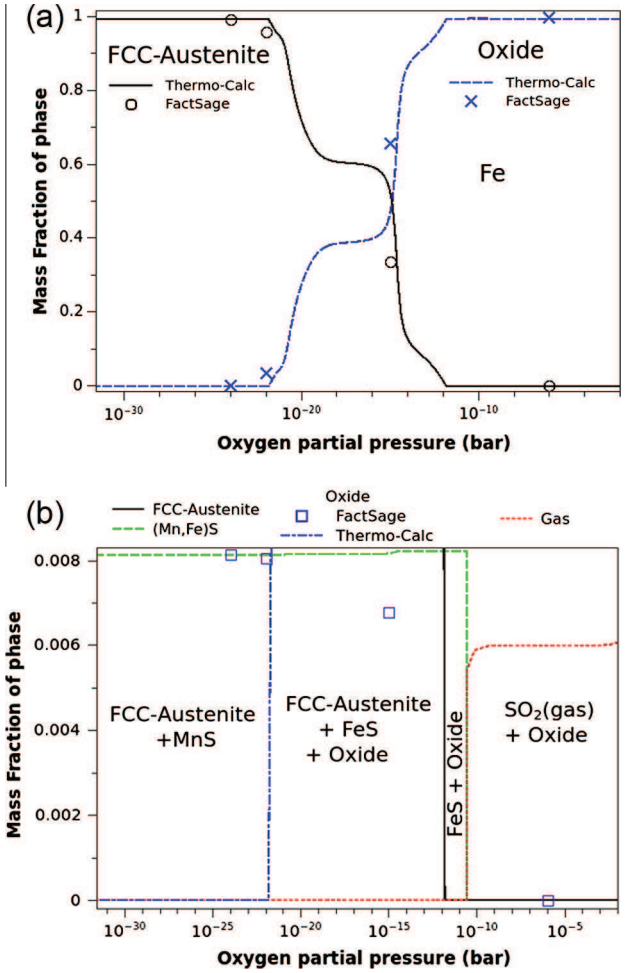

Fig. 10. Mass fraction of phases as a function of oxygen partial pressure (solid lines: calculations using Thermo-Calc with TCFE6 database [32,33], scatter plot: calculation using FactSage [36]): (a) austenite and oxide mass fractions, (b) S containing components mass fractions and sequence of successive phases from the bulk to the oxide depending on the oxygen partial pressure.

at the metal/oxide interface of chromia forming alloy seems to be a second order effect in the scale failure process [7,34].

Thermodynamic calculations concerning the high S grade, AISI 303, were achieved in order to determine the most stable phase containing S. Although some metallic sulphides and oxysulphides are not taken into account in the TCFE6 database, Thermo-Calc can be used to evaluate the mass fraction of phases in equilibrium and the chemical composition of each phase as a function of the oxygen partial pressure, $p(O_2)$. The diagrams points calculated with FactSage are also plotted to compare the results obtained using the two softwares [35,36].

The mass fractions of the two main phases in equilibrium at 1000 °C in synthetic air in AISI 303 are displayed in Fig. 10. The two main phases are the metallic FCC-austenite phase for low $p(O_2)$ and an oxide for the high $p(O_2)$ (Fig. 10(a)).

Presence of MnS and FeS is observed for low $p(O_2)$ and the formation of gaseous SO_2 provided by sulphide oxidation is predicted

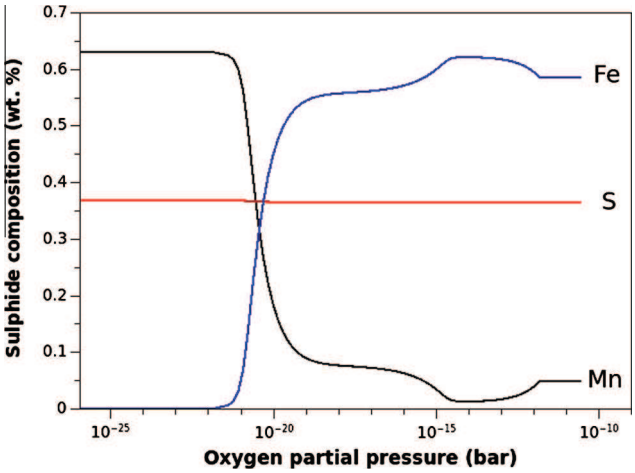

Fig. 11. Chemical composition of metallic sulphides in wt.% as a function of oxygen partial pressure calculated using Thermo-Calc with TCFE6 database [32,33].

for high $p(O_2)$ (i.e. $p(O_2) > 10^{-11}$ bar in Fig. 10(b)). The equilibrium sulphide compositions at 1000 °C in AISI 303 are displayed in Fig. 11. For $p(O_2)$ lower than 10^{-22} bar, S is mainly present as MnS inclusions in the bulk since the solubility of elementary S in the FCC-austenite phase is very low (Table 2). For $p(O_2)$ higher than 10^{-22} bar, MnS is oxidized. Whereas Mn is included in the spinel oxide $(Cr,Mn)_3O_4$, S is trapped by Fe to form iron sulphide (FeS). From these thermodynamic calculations, the sequence of successive phases from the bulk to the oxide depending on the oxygen partial pressure (i.e. for increasing $p(O_2)$) is: [FCC-austenite + MnS]/[FCC-austenite + FeS + oxide]/[FeS + oxide]/[oxide + SO_2 gas] (Fig. 10(b)).

The formation of Cr,Mn-rich oxysulphides cannot be foreseen because only MnS and FeS sulphides are taken into account in TCFE6 database. The experimental observations show that the oxidation of MnS gives rise to the formation of more stable Mn,Cr-rich oxysulphides instead of the predicted FeS. Thermodynamic calculations also predict the formation of gaseous SO_2 phase for $p(O_2)$ above 10^{-11} bar from the oxidation of FeS (Fig. 10(b)). However, sulphides and oxysulphides are internal precipitates beneath the oxide layer and the oxygen partial pressure is not high enough to oxidize these precipitates, so we assume that the release of SO_2 gas cannot explain the scale failure.

From our experimental results and thermodynamic calculations a scenario can be proposed. MnS inclusions near the metal/oxide interface are partially dissociated during thermal processing. Whereas Mn diffuses to the metal/oxide interface and is incorporated in the oxide scale, S is mainly trapped in the form of Mn,Cr-rich oxysulphides. The formation of these Mn,Cr-rich oxysulphides near the oxide/scale interface ties up the Cr. This leads to the strengthening of Cr depletion in the bulk below the oxide scale. The Cr concentration underneath the oxide scale decreases below the critical value which allows the formation of a continuous Cr-rich oxide layer. The formation of fast growing Fe-rich oxides is then promoted. It results in the formation of Fe-rich oxide pits underneath the Cr-rich oxide scale. Eventually, as the Fe-rich pit grows inward the alloys depth, the Cr concentration at the base of the pit increases until reaching a level high enough to sustain again the growth of a continuous Cr-rich oxide. Fe-rich oxides are undercut by a Cr-rich layer which causes a decrease of the oxidation rate. This mechanism is repeated several times leading to the formation of nodules mainly composed of alternated Fe-rich and Cr-rich oxides scales resulting in breakaway oxidation of AISI 303 in our experimental conditions. This description is illustrated in Fig. 12. In order to simplify the description, the oxysulphides, observed experimentally, are assimilated to sulphides.

4. Conclusions

AISI 304L and AISI 303 austenitic stainless steels were oxidized under severe experimental conditions, 1000 °C during 50 h in synthetic air flow. Although their initial microstructure and chemical composition are very close, except for S content, their oxidation behaviour differs strongly. The high S grade, AISI 303, presents catastrophic oxidation behaviour with a high oxidation rate and an extensive spalling event during cooling. Microstructural characterizations evidenced that the low S grade, AISI 304L, exhibits a fairly protective duplex oxide scale whereas breakaway oxidation happens for AISI 303 with the formation of nodules mainly composed of alternated Fe-rich and Cr-rich oxide scales. Thermodynamic calculations point out that free S content is independent of the S amount in the as-received alloy and thus is not responsible for breakaway oxidation of AISI 303. The increase in number and the decrease in size as well as the Cr enrichment and oxidation of the former MnS precipitates close to the metal/oxide interface suggest a dissociation of MnS inclusions during thermal processing. Whereas Mn diffuses to the metal/oxide interface and is incorporated in the oxide scale in the form of spinel oxide, the S is mainly trapped in the form of two-phase aggregates called Cr,Mn-oxysulphides which consist of Cr, Si-rich oxides and Mn, Cr-rich sulphides. The formation of these oxysulphides leads to a local decrease of the

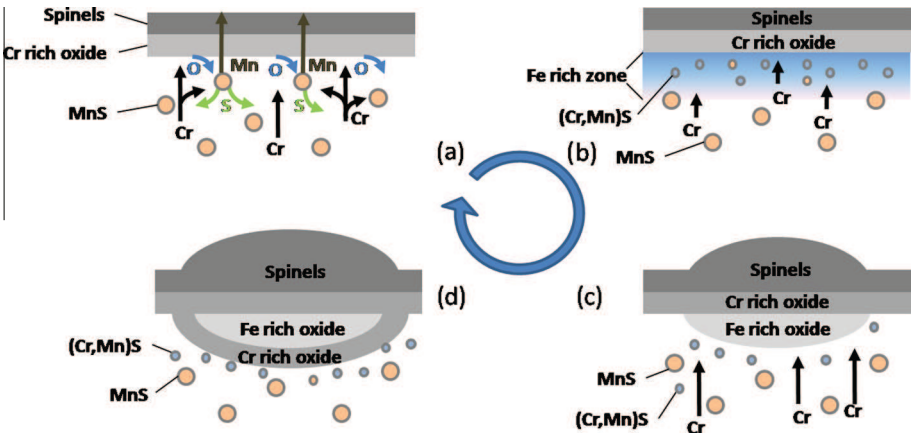

Fig. 12. Schematic of breakaway oxidation induced by alloyed sulphur.

Cr concentration under the oxide scale resulting in the breakaway oxidation of AISI 303 in our experimental conditions.

Acknowledgments

This work was realized in the framework of a PICS project supported by National Centre for Scientific Research (CNRS, France) Ref n° 6095 and Russian Foundation for Basic Research (RFBR) Ref n° 13-08-91053-CNRS_a.

References

[1] C. Trombert, Usanibilité des aciers inoxydables, Techniques de l'Ingénieur, m276, 1998.
[2] A.W. Funkenbusch, J.G. Smeggil, N.S. Bornstein, Reactive element-sulphur interaction and oxide scale adherence, Metall. Trans. A 16A (1985) 1164–1166.
[3] J.G. Smeggil, A.W. Funkenbush, N.S. Bornstein, A relationship between indigenous impurity elements and protective oxide scale adherence characteristics, Metall. Trans. A 17A (1986) 923–932.
[4] J.L. Smialek, Adherent Al_2O_3 scales formed on undoped NiCrAI alloys, Metall. Trans. A 18A (1987) 164–167.
[5] J.G. Smeggil, A.J. Shuskus, N.S. Bornstein, M.A. DeCrescente, The role of Active Elements in the Oxidation Behaviour of High Temperature Metals and Alloys, Springer, Netherlands, 1989.
[6] G. Dearnaley, The role of segregated impurities in scale adhesion, Corros. Sci. 32 (1991) 113–116.
[7] P.Y. Hou, J. Stringer, Oxide scale adhesion and impurity segregation at the scale/metal interface, Oxid. Met. 38 (1992) 323–345.
[8] T. Gheno, D. Monceau, D. Oquab, Y. Cadoret, Characterization of sulphur distribution in Ni-based superalloy and thermal barrier coating after high temperature oxidation: a SIMS analysis, Oxid. Met. 73 (2010) 95–113.
[9] Q. Li, X. Peng, J.Q. Zhang, G.X. Zong, F.H. Wang, Comparison of the oxidation of high-sulfur Ni–25Cr–5Al alloys in as-cast and as-sputtered states, Corros. Sci. 52 (2010) 1213–1221.
[10] D.W. Yun, S.M. Seo, H.W. Jeong, Y.S. Yoo, The cyclic oxidation behaviour of Ni-based superalloy GTD-111 with sulphur impurities at 1100 °C, Corros. Sci. 90 (2015) 392–401.
[11] S.N. Basu, G.J. Yurek, Effect of alloy grain size and silicon content on the oxidation of austenitic Fe–Cr–Ni–Mn–Si alloys in pure O_2, Oxid. Met. 36 (1991) 281–315.
[12] H.J. Grabke, D. Wiemer, H. Viefhaus, Segregation of sulphur during growth of oxide scales, Appl. Surf. Sci. 47 (1991) 243–250.
[13] V.K. Tolpygo, H. Viefhaus, Segregation at the Al_2O_3-FeCrAl interface during high-temperature oxidation, Oxid. Met. 52 (1999) 1–29.
[14] D. Monceau, B. Pieraggi, Determination of parabolic rate constants from a local analysis of mass-gain curves, Oxid. Met. 50 (1998) 477–493.
[15] F. Riffard, H. Buscail, E. Caudron, R. Cueff, C. Issartel, S. Perrier, Yttrium implantation effect on 304L stainless steel high temperature oxidation at 1000 °C, J. Mater. Sci 37 (2002) 3925–3933.
[16] D. Lussana, D. Baldissin, M. Massazza, M. Baricco, Thermodynamic and kinetics aspects of high temperature oxidation on a 304L stainless steel, Oxid. Met. 81 (2014) 515–528.
[17] A. Raffaitin, D. Monceau, E. Andrieu, F. Crabos, Cyclic oxidation of coated and uncoated single-crystal nickel-based superalloy MC2 analyzed by continuous thermogravimetry analysis, Acta Mater. 54 (2006) 4473–4487.
[18] G.J. Yurek, D. Eisen, A. Garratt-Reed, Oxidation behavior of a fine-grained rapidly solidified 18–8 stainless steel, Metall. Trans. A 13A (1982) 473–485.
[19] E. Fedorova, M. Braccini, D. Monceau, D. Oquab, V. Parry, M. Mantel, C. Pascal, Y. Wouters, High Temperature Oxidation of Austenitic Stainless Steels in Relation with the Oxide/Metal Interfacial Behavior During Tensile Test, in: Book of Abstracts of 18th International Symposium on the Reactivity of Solids (ISRS-18), St-Petersbourg, 2014, pp. 213–214.
[20] J.-P. Petit, M. Mermoux, Y. Wouters, A. Galerie, C. Chemarin, Study of the thermal oxidation of Fe-15 Cr by combined Raman and photoelectrochemical imaging, Mater. Sci. Forum 461–464 (2004) 681–688.
[21] I. Saeki, T. Saito, R. Furuichi, H. Konno, T. Nakamura, K. Mabuchi, M. Itoh, Growth process of protective oxides formed on type 304 and 430 stainless steels at 1273 K, Corros. Sci. 40 (8) (1998) 1295–1302.
[22] M. Jepson, PhD thesis, Loughborough University, Loughborough, 2008.
[23] T. Gheno, D. Monceau, D.J. Young, Mechanism of breakaway oxidation of Fe–Cr and Fe–Cr–Ni alloys in dry and wet carbon dioxide, Corros. Sci. 64 (2012) 222–233.
[24] H.E. Evans, D.A. Hilton, R.A. Holm, S.J. Webster, The development of localized pits during stainless steel oxidation, Oxid. Met. 14 (1980) 235–247.
[25] R.C. Lobb, H.E. Evans, An evaluation of the effect of surface chromium concentration on the oxidation of a stainless steel, Corros. Sci. 23 (1) (1983) 55–73.
[26] G. Bamba, Y. Wouters, A. Galerie, F. Charlot, A. Dellali, Thermal oxidation kinetics and oxide scale adhesion of Fe–15Cr alloys as a function of their silicon content, Acta Mater. 54 (15) (2006) 3917–3922.
[27] Lu Liu, Zhi-gang Yang, Chi Zhang, Mitsutoshi Ueda, Kenichi Kawamura, Toshio Maruyama, Effect of grain size on the oxidation of Fe–13Cr–5Ni alloy at 973 K in Ar–21 vol%O_2, Corros. Sci. 91 (2015) 195–202.
[28] D.F. Susan, J.A. Van Den Avyle, S.L. Monroe, N.R. Sorensen, B.B. McKenzie, J.E. Christensen, J.R. Michael, C.A. Walker, The effects of pre-oxidation and alloy chemistry of austenitic stainless steels on glass/metal sealing, Oxid. Met. 73 (2010) 311–335.
[29] W.S. Rasband, ImageJ, U.S. National Institute of Health, Bethesda, Maryland, USA, http://imagej.nih.gov/ij:, 1997–2014.
[30] J. Lehmann, Application of ArcelorMittal Maizières thermodynamic models to liquid steel elaboration, Rev. Metall. 105 (2008) 539–550.
[31] H.L. Lukas, S.G. Fries, B. Sundman, Computational Thermodynamics-The Calphad Method, Cambridge University Press, 2007.
[32] Thermo-Calc TCCS Version S, ThermoCalc Software AB, Stockholm, Sweden. http://www.thermocalc.com.
[33] TCFE6 – TCS steels/Fe-alloys database, version 6.2, Thermo-Calc Software AB, Stockholm, Sweden, 2009.
[34] F.H. Stott, G.C. Wood, J. Stringer, The influence of alloying elements on the development and maintenance of protective scales, Oxid. Met. 44 (1995) 113–145.
[35] C.W. Bale, E. Bélisle, P. Chartrand, S.A. Decterov, G. Eriksson, K. Hack, I.-H. Jung, Y.-B. Kang, J. Melançon, A.D. Pelton, C. Robelin, S. Petersen, FactSage thermochemical software and databases – recent developments, CalPhad 33 (2009) 295–311.
[36] FactSage 6.2 Thermochemical Software, Thermfact and GTT-Technologies, Center for Research in Computational Thermochemistry, Montreal, Canada, 2009.